

Folding Large Graphene-on-Polymer Films Yields Laminated Composites with Enhanced Mechanical Performance

Bin Wang, Zhancheng Li, Chunhui Wang, Stefano Signetti, Benjamin V. Cuning, Xiaozhong Wu, Yuan Huang, Yi Jiang, Haofei Shi, Seunghwa Ryu, Nicola M. Pugno, and Rodney S. Ruoff**

A folding technique is reported to incorporate large-area monolayer graphene films in polymer composites for mechanical reinforcement. Compared with the classic stacking method, the folding strategy results in further stiffening, strengthening, and toughening of the composite. By using a water–air-interface-facilitated procedure, an A5-size 400 nm thin polycarbonate (PC) film is folded in half 10 times to a ≈ 0.4 mm thick material (1024 layers). A large PC/graphene film is also folded by the same process, resulting in a composite with graphene distributed uniformly. A three-point bending test is performed to study the mechanical performance of the composites. With a low volume fraction of graphene (0.085%), the Young's modulus, strength, and toughness modulus are enhanced in the folded composite by an average of 73.5%, 73.2%, and 59.1%, respectively, versus the pristine stacked polymer films, or 40.2%, 38.5%, and 37.3% versus the folded polymer film, proving a remarkable mechanical reinforcement from the combined folding and reinforcement of graphene. These results are rationalized with combined theoretical and computational analyses, which also allow the synergistic behavior between the reinforcement and folding to be quantified. The folding approach could be extended/applied to other 2D nanomaterials to design and make macroscale laminated composites with enhanced mechanical properties.

Graphene oxide or reduced graphene oxide has seen wide use as a filler in composite materials as it can achieve significant mechanical enhancement with minimal volume of filling due to its mechanical properties and atomic thickness.^[1–5]

However, performance in some situations could be limited by defects (holes simply put) in the graphene oxide platelets. Furthermore, its incorporation in composite materials is typically with a random orientation that could limit mechanical

Dr. B. Wang, Dr. C. Wang, Dr. B. V. Cuning, Dr. X. Wu, Dr. Y. Huang, Dr. Y. Jiang, Prof. R. S. Ruoff
Center for Multidimensional Carbon Materials
Institute for Basic Science (IBS)
Ulsan 44919, Republic of Korea
E-mail: rsruoff@ibs.re.kr, ruofflab@gmail.com

Prof. Z. Li, Prof. H. Shi
Chongqing Institute of Green and Intelligent Technology
Chinese Academy of Sciences
Chongqing 400714, P. R. China

Dr. S. Signetti, Prof. S. Ryu
Department of Mechanical Engineering
Korea Advanced Institute of Science and Technology (KAIST)
Daejeon 34141, Republic of Korea

Prof. N. M. Pugno
Laboratory of Bio-Inspired & Graphene Nanomechanics
Department of Civil
Environmental and Mechanical Engineering
University of Trento
Via Mesiano 77, 38123 Trento, Italy
E-mail: nicola.pugno@unitn.it

 The ORCID identification number(s) for the author(s) of this article can be found under <https://doi.org/10.1002/adma.201707449>.

Prof. N. M. Pugno
School of Engineering and Materials Science
Queen Mary University of London
Mile End Road, London E1 4NS, UK

Prof. N. M. Pugno
Ket-Lab
Eduardo Amaldi Foundation
Italian Space Agency
Via del Politecnico snc
00133 Rome, Italy

Prof. R. S. Ruoff
Department of Chemistry
Ulsan National Institute of Science and Technology (UNIST)
Ulsan 44919, Republic of Korea

Prof. R. S. Ruoff
School of Materials Science and Engineering
Ulsan National Institute of Science and Technology (UNIST)
Ulsan 44919, Republic of Korea

DOI: 10.1002/adma.201707449

reinforcement for certain applications when compared to having, say, platelets aligned in preferred directions.^[6–10] Alternatively, the growth of large area, monolayer graphene on copper foils (by chemical vapor deposition, CVD) is now providing large, continuous, and high-quality graphene films, thus as a new candidate for mechanical reinforcement.^[11–15] Incorporating large area but atomically thin monolayer CVD-grown graphene films into composite materials while simultaneously preserving their structure is essential to optimizing composite mechanics. Recently, inclusion of graphene monolayers into polycarbonate (PC)^[16] or poly(methyl methacrylate) (PMMA)^[17] composites at quite low volume fraction by a stacking approach resulted in a significant increase in elastic modulus, as measured by uniaxial tensile tests.

Here, to further strengthen the laminated composite, folding, rather than stacking of separated layers, is used to make a macroscale composite. Bending tests were used to measure the mechanical properties, while the combination of theoretical prediction and finite element method (FEM) numerical modeling allowed us to demonstrate and quantify the synergistic effect by both the presence of graphene and folding, on the enhancement of the reported mechanical properties. Having one continuous graphene folded multiple times within the matrix yields a different type of structure with respect to simple matrix-graphene-stacked laminate with disconnected graphene layers. The fold plays a special role in stiffening and strengthening the composite. The folded structure can sustain a larger bending force as compared with the analog of stacked but disconnected layers, which could be explained by the improved layer–layer interaction generated from the additional constraint(s) by the folds.

In particular, the bending stiffness of a plate composed of n perfectly bonded layers of linear, elastic, homogeneous, and isotropic material is^[18]

$$D_n = \frac{E(nt)^3}{12(1-\nu^2)} = n^3 D_1 \quad (1)$$

where E is the Young's modulus of the material, ν its Poisson's ratio, and t the thickness of the layer. Vice versa, for noninteracting layers, the total bending stiffness is by definition $D_n = nD_1$.^[18] Thus, in general $D_n = n^\alpha D_1$ and we expect the following scaling for the nominal Young's bending modulus ($\propto D_n/n^3$)^[18]

$$E_n \cong E_1 n^{\alpha-3} \quad (2)$$

where $1 \leq \alpha \leq 3$ describes the interaction between the composite layers. Thus, the bending modulus of the laminated composite with and without folds is related to the interlayer interaction.

For the composite with a single layer graphene, the following rule of mixture holds

$$E_1 \cong E_g \frac{t_g}{t_g + t_m} + E_m \frac{t_m}{t_g + t_m} \quad (3)$$

where $E_{g,m}$ are the graphene/matrix Young's moduli and $t_{g,m}$ are the graphene/matrix thicknesses in the single layer with

$t_g + t_m = t$. The two phases within a single layer are assumed to be perfectly bonded. Minimizing the value of t_m as well as maximizing the interaction between the layers, i.e., the α exponent, are the two strategies for maximizing the bending modulus of the folded graphene composite, with the theoretical value predicted to be

$$E_{1,\text{ideal}} \cong E_g \frac{t_g}{t_g + t_{m,\text{min}}} \quad (4)$$

for $E_g \gg E_m$; whereas for $\alpha \rightarrow 3$ $E_n = E_1$; we expect $t_{m,\text{min}}$ in the nanometer range (theoretically, for $t_{m,\text{min}} = 0$ we obviously have $E_{1,\text{ideal}} = E_g$). Equations (2) and (3) can be combined to predict a stiffening of the folded composite due to the presence of the folding and graphene, according to

$$E_n^{(F,G)} = s_E f_E E_1 = s_E f_E g_E E_m \quad (5)$$

with $f_E g_E > 1$, where $f_E = n^{\alpha_f - \alpha}$ and α_f denotes the exponent of Equation (2) in the presence of folding (larger than its non-folded counterpart α) and $g_E = \frac{E_g}{E_m} \frac{t_g}{t_g + t_m} + \frac{t_m}{t_g + t_m}$ from

Equation (3); $s_E > 1$ is a factor which quantifies the mutual synergy between graphene reinforcement and folding process, as emerges from experiments.

According to fracture mechanics,^[18] we expect a scaling of the delamination strength, which is responsible for the failure of our specimens and thus can be considered as the ultimate strength of the multilayer, as $\sigma_u \propto \sqrt{E\gamma_C}$ where $2\gamma_C$ is the fracture energy of the interface, also expected to depend on the presence of folding and/or graphene reinforcement, i.e., $\gamma_C^{(F,G)} = \gamma_C s_\gamma f_\gamma g_\gamma$, where $s_\gamma f_\gamma g_\gamma > 1$ denotes the related synergy toughening mechanism due to folding and the graphene, respectively. The corresponding relations are shown as Equations (S1)–(S3) in the Supporting Information. The synergy factors, which are defined analogously as for the bending modulus, account for further enhancement of different properties due to beneficial interaction of reinforcement and folding process, as actually was observed in our experiments (see Table S1 in the Supporting Information). The previous equations will be applied for comparison with experimental values (see Table S2 in the Supporting Information)

To build a 3D material from 2D films by folding, paper origami provides a good example. It has been reported that A4 paper is difficult to fold (in half) more than 8 times, as the energy required for further folding increases rapidly.^[19] Gallivan folded a 1200 m long sheet of paper in half 12 times.^[19] To the best of our knowledge folding of nanoscale thin films many times has not yet been achieved. Very recently, we invented a method to realize 1 fold of monolayer CVD-grown graphene by using the surface of water to support the graphene; this method can be readily used for the folding of other large and thin 2D films.^[20]

In this work, we folded ≈ 400 nm thick A5-sized (21 cm \times 15 cm) PC films in half 10 times, yielding an ≈ 0.4 mm thick bulk “beam-like” sample with 1024 layers that had lateral dimensions of 2.6 cm \times 0.11 cm. Through a simple modification of the procedure, PC on graphene films could be produced which, when folded, yielded a PC/graphene composite; a

three-point bending test was then used to study the mechanical properties. Folding of either the pure PC film or the PC/graphene film resulted in enhanced mechanical properties compared to the nonfolded control samples. With a low volume fraction of graphene of 0.085%, the Young's modulus, strength, and toughness modulus were enhanced in the folded composite by an average of 73.5%, 73.2%, and 59.1%, respectively, as compared with the pristine stacked polymer films, or 40.2%, 38.5%, and 37.3% as compared with the folded polymer film.

The process for achieving 10 folds using the thin film was divided into two distinct steps: first 4 folds are performed with a patterned "substrate to enable folding" and water-assisted delamination of the relevant part, and then 6 more folds were made by manually folding the film in half each time. The first step is shown schematically in **Figure 1**, with details in the Experimental Section. A silicon wafer piece (24 cm × 20 cm) with a 300 nm thick thermal oxide layer was modified with a hydrophobic self-assembled monolayer (SAM) and used as the substrate for the folding. The SAM pattern was designed with several "folding lines" for the initial 4 folds of the sample, as shown in Figure S1 (Supporting Information). As we have demonstrated previously, this hydrophobic SAM-modified substrate surface allows the polymer film to adhere to the hydrophobic region when immersed in water and enables folding when the assembly is withdrawn from the water.^[21] An A5-sized (21 cm length × 15 cm width × 25 μm thick) polycrystalline Cu foil which had a PC layer spin-coated on its surface (PC-Cu) was then pressed onto this patterned substrate so that the substrate surface contacted with the PC layer. After etching away the Cu foil in aqueous etchant (0.2 M (NH₄)₂S₂O₈) and replacing the etchant with deionized water, the assembly was slowly withdrawn from the water, and the floating PC film which was previously pressed on the hydrophilic region of the folding substrate (region without the SAM) folded over the other half of the PC film along the 1st folding line to realize the 1st fold. Three further folds were performed by the same water-assisted process to yield a 4-fold PC film with 16 layers, which had sufficient strength to be peeled from the substrate without damage

for further manual folding. The steps of the folding process were recorded with photos, see Figure S2 (Supporting Information). After the 10th fold, the sample became too rigid to fold further. Then, it was compressed (≈40 MPa) in a machine press at 150 °C for 10 min to improve interlayer contact, yielding the folded bulk material with thickness around 0.4 mm, consisting of a total of 1024 layers of thin film PC. To find out how many folds could be achieved, we found that the compressed 10-fold sample could be folded 2 more times (12 folds; Figure S3, Supporting Information). However, this 12-fold sample was not studied further due to the need for a minimum sample size in our mechanical testing equipment.

To incorporate CVD-grown graphene in the composite, the same folding procedure described above was used, however prior to PC spin-coating, the large copper foil was first coated with a continuous single layer graphene (G) grown by CVD,^[12,22] thus producing a "PCG" film on the Cu foil. The thickness of a single layer PCG obtained by spin-coating a 4 wt% PC/chloroform solution on CVD-grown monolayer graphene film/Cu foil was measured using atomic force microscopy (AFM), as shown in Figure S4 (Supporting Information). The thickness is around 400 nm, which was the thinnest film for which we could reliably form the 1st fold of the A5-sized film without fracture in our experiments.

To compare the effect of folding (F) versus stacking (S), we also prepared samples by sequentially stacking individual layers of ≈400 nm thick PC both with (S-PCG) or without (S-PC) a single monolayer graphene film to compare their mechanical response to their folded counterparts, i.e., "F-PCG" or "F-PC" composites. Note that the S-PCG layers were stacked in a PC-G-G-PC sequence to maintain the same stacking order as the folded sample. All samples were hot pressed at 150 °C for 10 min at ≈40 MPa to densify the composite and promote the interfacial contact, prior to measurement at room temperature in ambient conditions.

Scanning electron microscopy (SEM) images in **Figure 2a,b** show the cross-section of S-PCG, where the closely stacked layered structure can be observed. A similar (appearing)

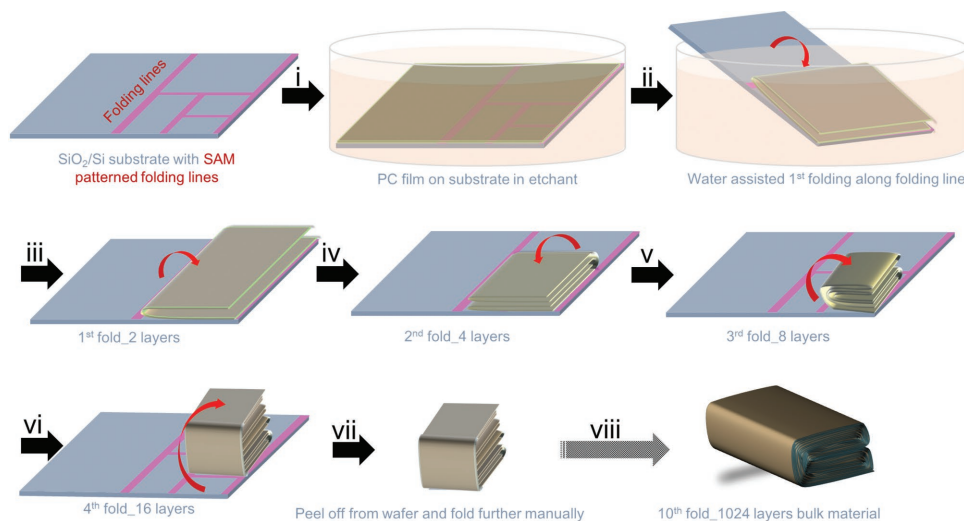


Figure 1. Schematic of the folding of an A5-sized ≈400 nm thick polycarbonate (PC) film, emphasizing the first four water-assisted folding steps that involve the use of a self-assembled-monolayer (SAM)-patterned substrate.

layered structure is also observed in the cross-section of **F-PCG** in Figure 2c, and the thickness of both samples was about 0.4 mm. The fold structure of **F-PCG** is shown in Figure 2d, where the vertically aligned and curved layers can be clearly observed. As compared with the horizontally stacked layers, these densely stacked vertical layers at the fold provide an additional constraint to the in-plane relative slip and normal separation of the layers, allowing the sample to sustain a larger bending force. Figure 2e shows the “continuously wrapped” configuration of the fold edge of the **F-PCG** sample, in comparison to the “open” layer edges in the case of **S-PCG** (Figure 2a). The volume fraction of graphene in the sample was estimated by accounting for the thickness of an individual layer of PC film, and the thickness of single layer graphene (assumed to be 0.34 nm) which yielded ≈ 0.085 vol% graphene.

To evaluate the graphene presence in the composites, Raman spectroscopy was used, see Figure 3 and Figure S5 (Supporting Information). The characteristic bands of PC appear at 1234.9, 1607.2, and 3075.1 cm^{-1} , representing the C–O, C=C, and methyl groups, respectively.^[16] With a single layer of graphene film on top of the PC film, the G (1587.2 cm^{-1}) and 2D (2676.3 cm^{-1}) bands for graphene are observed with negligible D band (≈ 1350 cm^{-1}), indicating the high quality of the monolayer graphene film. The inset in Figure 3a highlights the position difference of the G band of graphene and the C=C band

of PC which can be used for distinguishing graphene from PC. Figure 3b compares the spectra from the “plane” regions of the four bulk composites, in which **S-PC** and **F-PC** show pure PC signals, while **S-PCG** and **F-PCG** exhibit strong features of both PC and graphene. I_{2D}/I_G maps for 1 layer **PCG**, **S-PCG**, and **F-PCG** are compared in Figure S5 (Supporting Information). The I_{2D}/I_G ratio of ≈ 2 across the map for 1 layer **PCG** indicates the monolayer character of the graphene film on PC.^[23] I_{2D}/I_G values lower than 2 were observed in the maps for **S-PCG** and **F-PCG**, due to the twisted two graphene layers in these composites formed during the stacking and folding processes.^[23] Low and comparable D bands were detected for both **S-PCG** and **F-PCG** composites, corresponding to the I_D/I_G maps shown in Figure 3c,d. Defects were generated during “handling” of the graphene films, but the low intensity of the D band suggests that both stacking and folding processes preserved the high quality of the graphene films. Besides the “plane” regions for the composites, graphene quality in the “edge” regions was also measured by Raman maps, as shown in Figure 3e,f. High I_D/I_G intensity across the entire “edge” region for **S-PCG** shows the defects from the edges of graphene layers. In contrast, the graphene film is continuous at the fold of **F-PCG**, and thus low intensity of D band comparable to the “plane” region was observed in the “edge” region, indicating the high uniformity of graphene in **F-PCG**. Thus, folding process results in a multilayer composite with higher homogeneity of properties, avoiding the intrinsic weakness of edge regions.

To study the mechanical properties of the composite samples, bending tests were performed. A three-point bending configuration with a dynamic mechanical analysis (DMA) system was used, see Figure S6 (Supporting Information). The dimensions of the specimens were 15 mm \times ≈ 1.1 mm \times ≈ 0.4 mm (span \times width \times thickness, thus the span-to-thickness ratio is 37.5, based on the ASTM-D7264), and five specimens were measured for each composite configuration (Figure S7 and Table S2, Supporting Information). The loading tip had a cylindrical geometry and the radius was ≈ 0.3 mm. The length of the straight loading tip was 20 mm, much larger than the width of the specimens of 1.1 mm, resulting in a uniform contact with the specimen across its width. The maximum allowed deflection was 5 mm, thus the maximum strain resulting in the specimens was 5.3% (Equation (7)). The stress–strain plots were obtained by fixing the ramp displacement rate to 100 $\mu\text{m min}^{-1}$ and measuring the applied force and deflection.

In a three-point bending test, the failure of the specimen may occur due to either crack nucleation on the tensed surface (bottom chord) or to localized buckling and delamination or crushing at the compressed chord. The compressed chord of the beam is the surface that is in contact with the loading

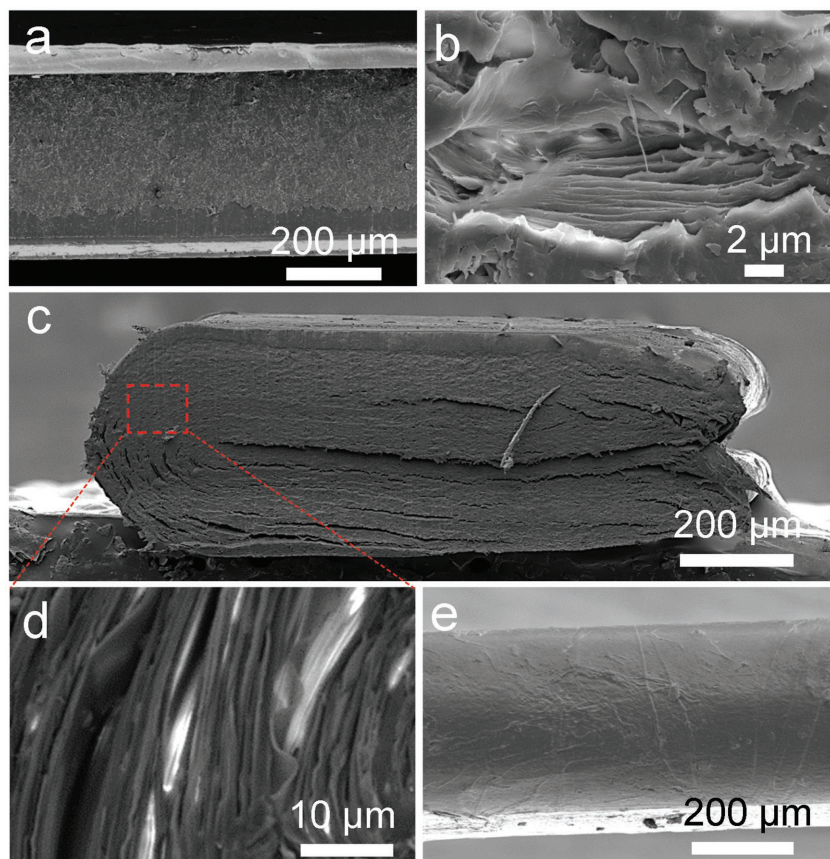


Figure 2. SEM images of the composite structures. a,b) Cross-section of 1024 stacked layers of **PCG** film (**S-PCG**), and c,d) cross-section of a **F-PCG** composite folded 10 times, and e) the fold edge (left side of the sample in (c)).

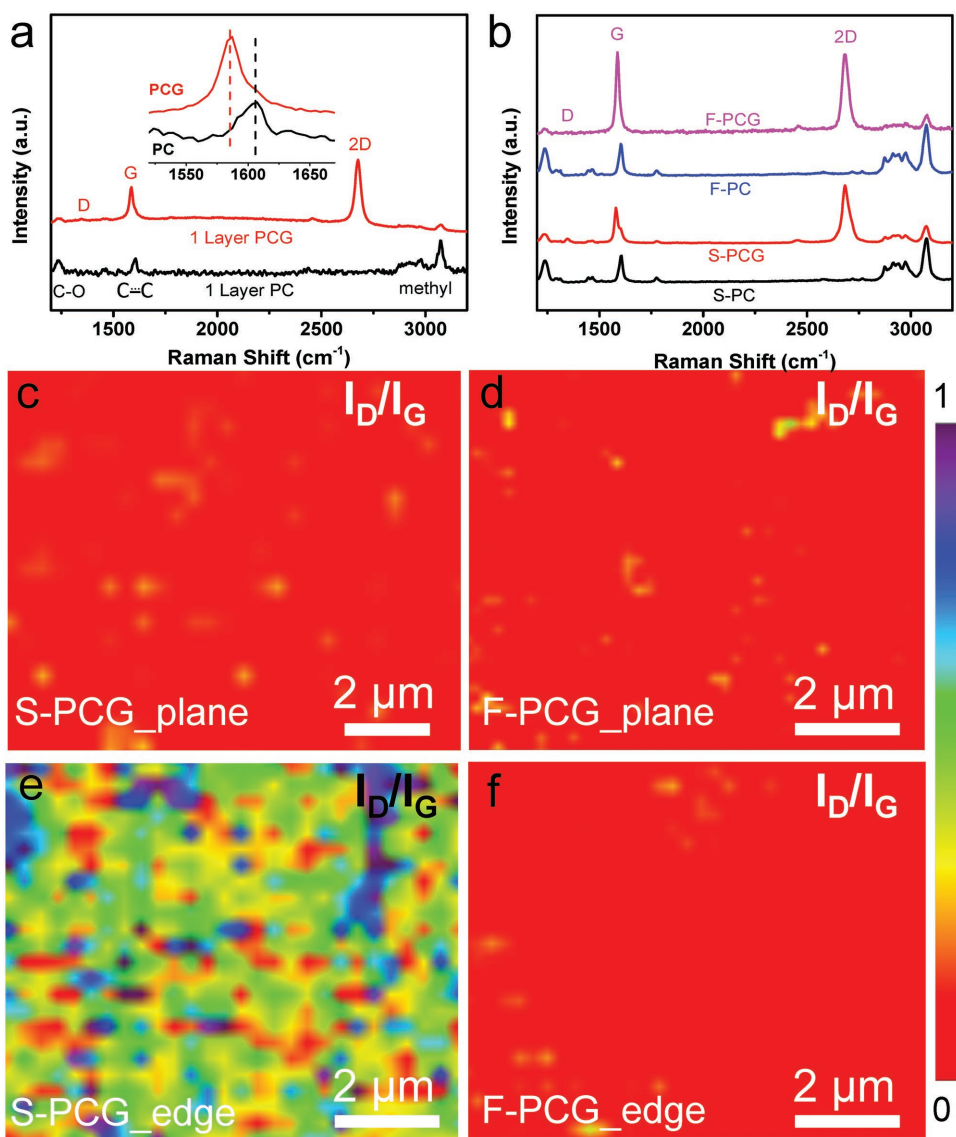


Figure 3. Raman spectroscopy of **S-PC**, **S-PCG**, **F-PC**, and **F-PCG** composites. a) Raman spectra of single layers of **PC** and **PCG**. The inset shows that the G band position of graphene in **PCG** and the C=C band of **PC** are distinguishable. b) Comparison of Raman spectra of the “plane” regions for the four tested multilayers. c–f) Raman maps of the intensity ratio of D to G bands (I_D/I_G) in the “plane” regions (c,d), and “edge” regions for **S-PCG** and **F-PCG** (e,f).

nose and thus opposite to the tensed chord. To convert the force–deflection to the stress–strain plot, the stress was calculated by

$$\sigma = \frac{3PL}{2bh^2} \quad (6)$$

where σ is the tensile stress at the bottom chord at mid-span, P is the external applied force, and L , b , and h , are the span, width, and thickness of the beam, respectively. The strain was calculated as

$$\varepsilon = \frac{6\delta h}{L^2} \quad (7)$$

where ε is the tensile strain at the bottom chord of the beam, and δ is the mid-span deflection. We used SEM to investigate the failure mechanism of the samples after bending tests, as shown in Figures S8 and S9 (Supporting Information). Cracks appeared on the tensed surface of the bent **S-PC** and **S-PCG** specimens, but no cracks were observed on the **F-PC** and **F-PCG** samples, indicating that the failure of the stacked samples was due to cracking of the tensed surface. On the other hand, no buckling was observed on the compressed surface for the **S-PC** and **S-PCG** specimens but appeared on the **F-PC** and **F-PCG** samples, indicating that the failure of the folded samples was due to buckling on the compressed surface.

The different failure mechanisms for the stacked and folded samples result from the different stress distributions from

bending that arise by different layer interactions from the folding, as shown in **Figure 4a**. By employing FEM simulations, we modeled the bending behavior of 4-fold, 5-fold, and 6-fold PC samples as compared with the corresponding stacked samples of 16 layers, 32 layers, and 64 layers. It was infeasible to directly model the 10-fold sample due to the high computational cost and the complexity in defining the boundary conditions to replicate folds (see the Experimental Section). Still, the simulation results enabled us to understand the effect of folding on the scaling of bending properties. As depicted in **Figure 4a**, the folded configuration provides much higher bending stiffness with respect to the stacked configuration due to the additional constraint given by the folds which results in enhanced layer mechanical interaction. This, consequently, results in both higher specific deformation energy stored in the plate, and also higher bending force (see **Figure S10** in the Supporting Information) at the same imposed displacement. The effective stress

on the folded regions (located at the edges and in the center of the samples) is approximately an order of magnitude higher than the stress in the mid-span of the stacked samples that is spread uniformly across the width of the sample. This higher effective stress is reflected on the load bearing capacity of the different layering configurations. A peripheral (at the sample edges) constraint due to folding allows the top layers to work in compression (as in a homogeneous bent beam), and the top layer is eventually delaminated and undergoes wrinkling. The simulation captures similar behavior observed in experiments (**Videos S2, S4, and S6**, Supporting Information). As a result, a much larger force and deformation energy are required to bend the folded samples with respect to the stacked samples, as depicted in **Figure 4b,c**.

In the stacked samples, the specific bending force and deformation energy are nearly constant irrespective of the number of layers, while they significantly increase with the number of

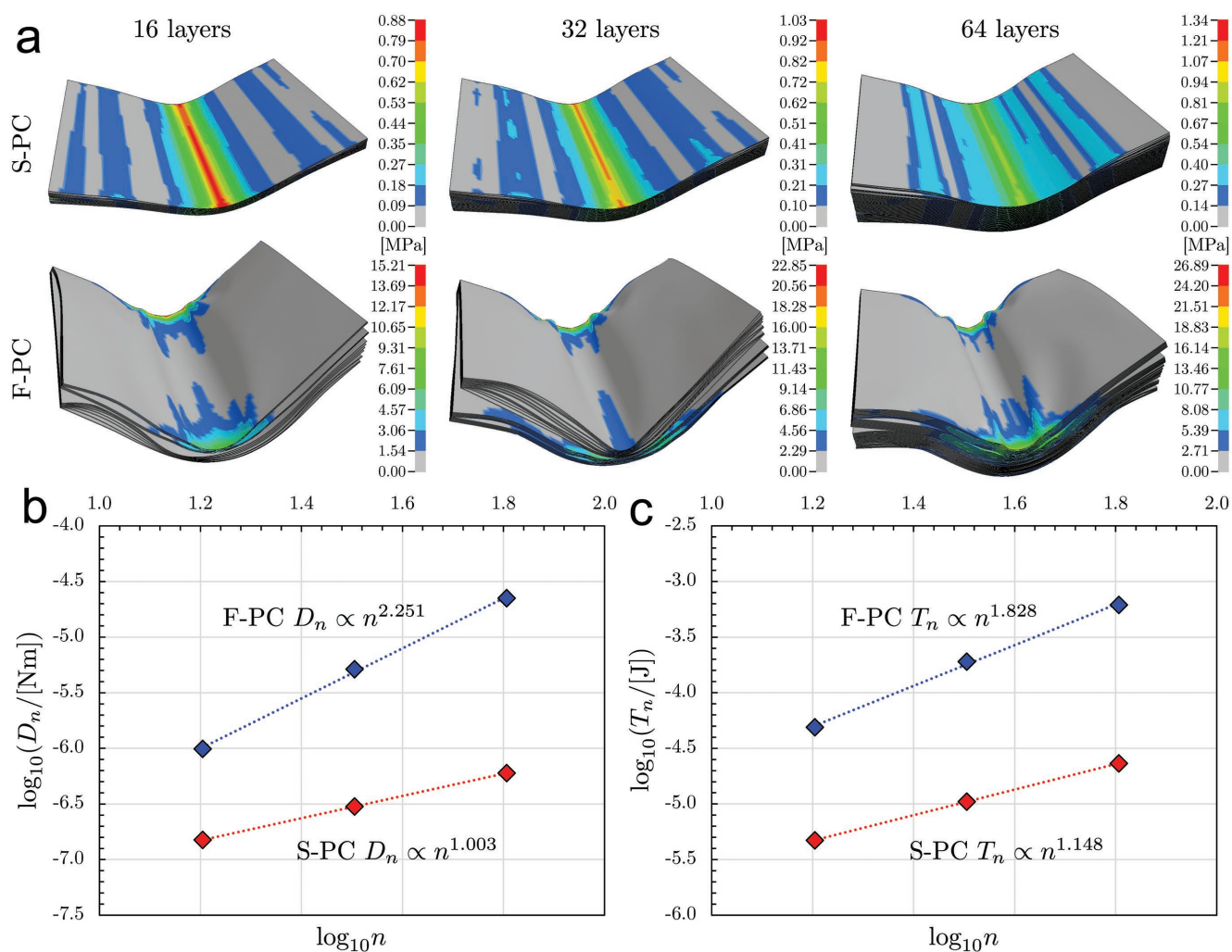


Figure 4. FEM three-point bending simulations on **S-PC** and **F-PC** samples, with $n = 16$ (4 folds), 32 (5 folds), and 64 (6 folds), aimed at discriminating the mechanical role of folding on the multilayer bending properties. **a**) Visual comparison of bending behavior of the samples with a contour plot of the von Mises stress within the specimen (units: MPa). Animations of the simulations are provided in **Videos S1–S6** (Supporting Information). **b**) Numerical scaling of the bending stiffness $D_n \propto n^\alpha$ (secant at 1 mm deflection), from where the theoretical power-law scaling dependencies are confirmed and the α , α_f power exponents can be extracted. **c**) Scaling of the specific deformation energy T_n (at 1 mm deflection). Complete simulation results (bending force, deformation energy, sliding interface energy) are reported in **Figure S10** (Supporting Information).

layers for the folded samples (Figure S10, Supporting Information). By computing the bending stiffness of **S-PC** and **F-PC**, we extract the exponent $\alpha_{F-PC} = 2.251$ that, in agreement with the theoretical prediction, lies in between the two limit cases of $\alpha_{S-PC} = 1$ (no bonding and actually observed in simulations of **S-PC** with different n , Figure 4b) and $\alpha = 3$ (perfect bonding/homogeneous beam). The exponent $\alpha_{F-PC} = 2.251$ is closer to the latter, demonstrating that folding is an effective strategy to produce a multilayer sample with enhanced mechanical properties closer to the limit of a perfectly homogeneous beam. Similar results are found by analyzing the deformation energy stored by the simulated samples. Since the internally stored energy at a given deflection δ is proportional to the product of the external applied force and the deflection, $T_n \propto P \cdot \delta$, and the force at a given deflection scales with n^α (the same as the bending stiffness, see Equation (1)), we expect similar scalings between the beam internal deformation energy and bending stiffness. In agreement with this prediction, the power-law behavior is clearly observed also for the strain energy and the related extracted exponents are $\alpha_{S-PC} = 1.148$ and $\alpha_{F-PC} = 1.828$, which are comparable to those determined from the bending stiffness. The observed difference is attributed to the fact that the deformation energy is affected by contact pressure at support/load points that increases with the stiffness of the beam. Also, the interface behavior is affected as the presence of folds increases the energy dissipated by friction (nearly 1/10 of the corresponding deformation energy, Figure S10, Supporting Information). This can be directly correlated to the complex relative displacement between layers induced

by the fold constraints (Figure 4a and Videos S2, S4, and S6 (Supporting Information)), indicating that the tailoring of interface parameters could further increase the load bearing capacity toward the ideal bulk beam value.

By comparing the stress–strain curves for **F-PC** and **S-PC** (Figure 5a), it was found that the folded composite showed an average (maximum) strength of 42.65 ± 3.08 MPa (47.61 MPa), which is higher than strength for the stacked composite of 34.12 ± 2.10 MPa (36.91 MPa), thus a larger load is required to fracture the **F-PC** composite (Figure 5b). A similar trend was observed in the cases for **F-PCG** and **S-PCG**, with strength, respectively, of 59.08 ± 6.41 MPa (64.56 MPa) and 41.03 ± 2.58 MPa (45.16 MPa), indicating that the difference in mechanical performance should depend on the difference in the structure of the composites, thus folded versus the stacked. The average (maximum) Young's modulus was: **F-PC** of 2.34 ± 0.14 GPa (2.52 GPa) versus **S-PC** of 1.89 ± 0.11 GPa (2.04 GPa), and **F-PCG** of 3.28 ± 0.24 GPa (3.58 GPa) versus **S-PCG** of 2.58 ± 0.19 GPa (2.78 GPa), see Figure 5c. The folded composite is much stiffer than the stacked composite. The toughness modulus between samples was obtained as the area under the stress–strain curve. In Figure 5d, the folded samples have larger average (maximum) toughness modulus values of 0.70 ± 0.16 MPa (0.86 MPa) for **F-PCG** and 0.51 ± 0.06 MPa (0.57 MPa) for **F-PC** than the stacked samples (0.40 ± 0.04 MPa (0.46 MPa) for **S-PCG** and 0.44 ± 0.04 MPa (0.48 MPa) for **S-PC**). The fracture strain values are comparable for all the samples, as shown in Figure S11 (Supporting Information).

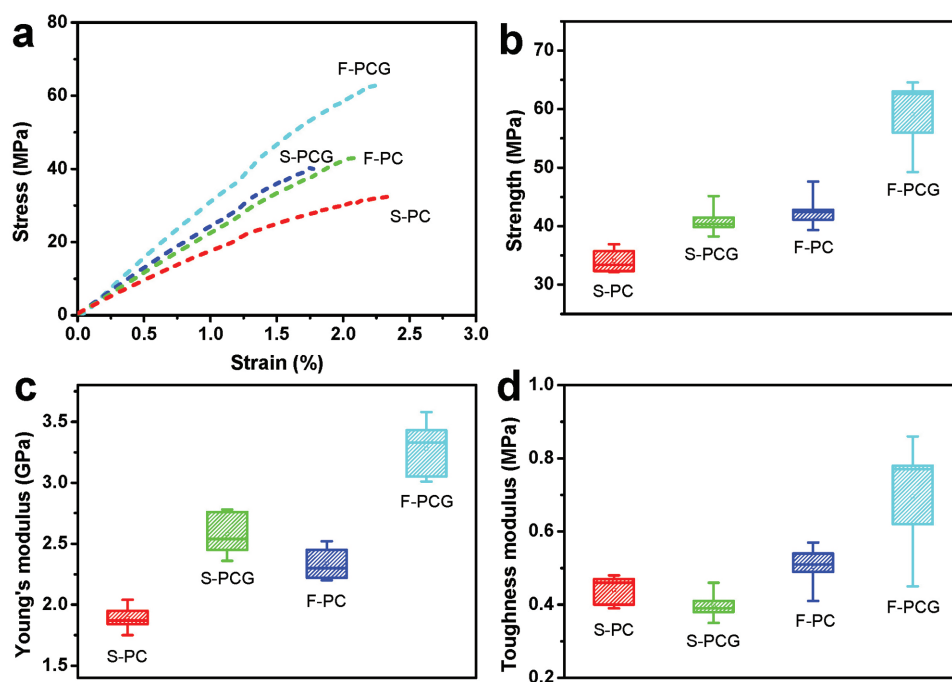


Figure 5. Mechanical test for the composites using three-point bending performed on dynamic mechanical analysis (DMA) equipment. a) Typical stress–strain responses under loading for different composites including **S-PC**, **S-PCG**, **F-PC**, and **F-PCG**. b–d) Statistic of fracture strength (b), Young's modulus (c), and toughness modulus (d) of different composites measured in ambient conditions. Five specimens were measured for each composite, and the summary of the as-measured mechanical properties is reported in Table S2 (Supporting Information), including maximum and average values also for the fracture strain. Note the superior mechanical characteristics for both maximum and average values of the **F-PCG** solution (with the exception of the fracture strain, see Figure S11, Table S2, and the “Model Predictions” section in the Supporting Information).

Besides the benefits from folding the PC film alone, filling with graphene further improves the mechanical performance of the composites. Despite the low volume fraction of 0.085% for graphene in the composites, the average (maximum) Young's modulus increased by 36.51% (36.27%) and 40.17% (42.06%), respectively, for **S-PCG** and **F-PCG**. By considering both the effects from folding and graphene filling, the Young's modulus, strength, and toughness modulus were enhanced by an average of 73.5%, 73.2%, and 59.1%, respectively, for the **F-PCG** composite as compared with **S-PC**, or 40.2%, 38.5%, and 37.3% as compared with **F-PC**, by considering only the reinforcement effect on the folded composite from graphene. We highlight this synergy by back-calculating the equivalent Young's modulus of the reinforcement E_g from rule of mixture of Equation (3) by exploiting experimental results (Table S2, Supporting Information). Assuming $E_m = 1.89$ GPa (average modulus from bending test on **S-PC**), from **S-PCG** samples (average $E_1 = 2.58$ GPa) we derive $E_g = 0.81$ TPa, which is comparable with the measured values for graphene as reported previously,^[24–26] analogously, we derive $E_g = 1.64$ TPa from **F-PCG** samples (average $E_1 = 3.28$ GPa). The latter value, which is somewhat higher than the ideal modulus of graphene (≈ 1 TPa), clearly quantifies the contribution given by the folding process in improving the mechanical properties of such nanocomposites. Similarly, for the back-calculated graphene strength, we found 8.17 GPa in absence of folding and 29.42 GPa in the presence of folding, again a significant fraction of the graphene ideal strength (≈ 100 GPa).

As a control experiment, we prepared a **PCG** sample using a melt process (**Melt-PCG**). Briefly, a **PCG** film of the same dimensions as those used in the stacked and folded samples was crumpled and then melted on a hot plate at 300 °C. Using the same thickness for the film ensured the same graphene-to-polymer ratio of the stacked and folded multilayers. After cooling, the **PC/graphene** melt was hot pressed (40 MPa) at 150 °C for 10 min to obtain films with a thickness of 0.4 mm. These films were then cut to obtain samples with the same beam geometry as the folded and stacked samples. The mechanical responses of these samples are shown in Figure S12 (Supporting Information). The average values are: Young's modulus of 2.29 ± 0.18 GPa, fracture strength of 43.53 ± 3.54 MPa, and toughness modulus of 0.54 ± 0.07 MPa (Table S3, Supporting Information). These values are all much lower than those for **F-PCG**, further indicating the advantages of folding the embedded graphene over other established processes.

For a comparison between experiments and model predictions, we use Equation (5) and Equations (S1)–(S3) (Supporting Information), finding a good agreement with $f_E \approx 1.242$, $g_E \approx 1.372$, $f_\sigma \approx 1.254$, and $g_\sigma \approx 1.208$, see the “Model Predictions” section and Table S2 (Supporting Information). Such a model could thus guide the design of similar types of multilayered composites. Finally, we note that the extracted value of g_E is in good agreement with the prediction of Equation (3) which yields $g_E \approx 1.449$, with $E_m = 1.89$ GPa (average modulus from bending test on **S-PC**). From analysis of experimental tests with our model, we also derived the global synergy factors $s_E \approx 1.023$, $s_\sigma \approx 1.146$, $s_\varepsilon \approx 1.261$, and $s_\gamma \approx 1.521$, which demonstrate and quantify how the reinforcing with 2D materials and the folding process mutually strengthen their contribution to

further enhance mechanical properties. Indeed, from our experiments, the average Young's modulus for **S-PCG** and **F-PCG** are 2.58 ± 0.19 and 3.28 ± 0.24 GPa, and the maximum values are 2.78 and 3.58 GPa, respectively, which are higher than the prediction of a simple rule of mixture. Moreover, recalling that $f_E = n^{\alpha_f - \alpha}$, we derive from experimental results (Table S2, Supporting Information) $\alpha_f - \alpha = 0.0313$ and assuming the simulation-derived scaling exponent ($\alpha_f = 2.251$), we obtain $\alpha = 2.222$. This value cannot be compared with the nearly negligible value for **S-PC** samples from the simulations, where we have deliberately reduced all the layer–layer interactions – adhesive energy fixed to be null with layers (apart normal contact and friction), which are nearly independent – to let the mere role of folding emerge. The low estimated exponent difference $\alpha_f - \alpha$ indicates a limited effect of folding in tested specimens. This can be explained by the role of adhesive interaction: in tested **PCG** sample, the adhesion energy between the layers was also high in the stacked sample, hence the limited improvement, while in our simulations, the contribution of folds is consequently more evident. The results show how the contribution of folding is much more useful in case of weak interfaces, for example, to counteract the presence of impurities or size-scale effects on adhesive interactions (low ratio between surface and volume forces), e.g., for the production of large-scale composites. Thus, the fold effect could be understood as an enhanced layer–layer interaction as compared with the stacked layers, yielding improved mechanical properties.

Here we also note that the thickness of polymer and the number of graphene layers may also affect the mechanical properties of the composite. Theoretically, reducing the thickness of the polymer by a factor p and increasing the number q of graphene layers, considering for the Young's modulus of the graphene multilayer the same Equation (2) with an exponent α_g ($n \rightarrow q$), would result in $g_E(p, q) \approx g_E(1, 1) \frac{p}{q^{2-\alpha_g}}$ ($E_g \gg E_m$, $t_m \gg t_g$).

Considering the intermediate value of $\alpha_g \approx 2$ ^[18,27] suggests that the number of graphene layers is not affecting the results and thus is not as important as the polymer thickness. For example, by reducing the polymer thickness by a factor of 4 would result in a stiffening by a factor of 4, a strengthening by a factor of 2, a reduction in the maximal strain by a factor of 2, and in an invariant toughness modulus. Therefore, the mechanical performance of the composite could be enhanced greatly by further reducing the thickness of polymer layer, although we have already used the thinnest **PC** film of 400 nm that we could fold without damage in this work.

In summary, folding was demonstrated to be an effective way to embed graphene in a polymer composite for achieving a high homogeneous multilayer with enhanced mechanical properties, providing a more effective reinforcement to the composite than simply stacked layers. Beyond the extreme alignment between graphene and polymer layers that can be realized by stacking, folding provides extra constraint(s) within the plate, resulting in additional stiffening, strengthening, and toughening of the composite. A water-based technique was used to fold an A5-sized polycarbonate film in half 4 times followed by manual folding 6 more times, from a single layer film of 400 nm thick to an ≈ 0.4 mm thick bulk material with 1024 layers. This method was also used to embed

monolayer graphene film into a composite structure which also has 1024 layers and similar overall thickness, thus forming a new type of composite with graphene. Even with a low volume fraction of graphene of 0.085% in the folded composite, the Young's modulus, strength, and toughness modulus were enhanced by an average of 73.5%, 73.2%, and 59.1%, respectively, as compared with the pristine stacked polymer films. In the stacked samples, the incorporation of graphene resulted in the enhanced Young's modulus of 36.5%, strength of 20.3%, and comparable toughness moduli, while these enhancements were 40.2%, 38.5%, and 37.3%, respectively, in the folded samples with the same volume percentage of graphene. The contribution of graphene reinforcement was thus increased by the folding, indicating a synergistic reinforcement mechanism from both folding and graphene, as quantified by the synergy factors. The models presented in this work could be helpful for the design of 2D material embedded in multilayered 3D composites, which can be realized at large size such as the experimental methods described in this work. Our synergistically enhanced graphene-reinforced composites made by folding are able to exploit the ideal properties of graphene and could thus be potentially applied on large scale in the aerospace and automotive industries. Furthermore, by combining various 2D materials that contribute special functionality, folding can be used to obtain macroscale materials for many other potential applications, including, but not limited to, energy storage and conversion, and thermal management.

Experimental Section

Patterning Substrate by SAMs: $\text{CF}_3(\text{CF}_2)_5(\text{CH}_2)_2\text{SiCl}_3$ (trichloro-(1*H*,1*H*,2*H*,2*H*-perfluorooctyl)silane), was used to form a SAM pattern on a silicon wafer (24 cm \times 20 cm) having a 300 nm thick thermally oxidized surface. The SiO_2/Si substrate was first exposed to O_2 plasma for 10 min to modify the surface with silanol groups ($-\text{Si}-\text{OH}$) for further reaction with $\text{CF}_3(\text{CF}_2)_5(\text{CH}_2)_2\text{SiCl}_3$, then PET films were used as masks to cover the surface regions where no modification by SAM was wanted. $\text{CF}_3(\text{CF}_2)_5(\text{CH}_2)_2\text{SiCl}_3$ (50 μL) was added to a vial and put into a vacuum desiccator together with the wafer and left for 12 h at room temperature to deposit the SAM molecules on those regions not covered by PET film. Then, the PET film regions were peeled from the wafer and those regions not covered by PET film formed a SAM pattern (hydrophobic) with the other hydrophilic regions. The patterned substrate was rinsed with ethanol and dried with nitrogen before use. The pattern design is shown in Figure 1 and Figure S1 (Supporting Information).

Folding Process: The 10 times folding process was divided to two steps: the first 4 folds were achieved by the transfer/folding on water using the patterned substrate, and then 6 more folds were done manually. A 4 wt% PC/chloroform solution was spin-coated on an A5-sized (21 cm \times 15 cm) Cu foil at 5000 rpm to form a PC film with thickness of about 400 nm. PC used here was poly(bisphenol A carbonate) from Sigma-Aldrich (average $M_w \approx 45\,000$). Then, the PC-coated Cu foil (**PC-Cu**) was pressed onto the patterned substrate so that the substrate surface contacted the PC layer. After etching away the Cu foil in the aqueous etchant (0.2 mol ammonium persulfate) and replacing the etchant with pure water, the assembly was slowly withdrawn from water, and the floating PC film (that had been on the hydrophilic region (no SAM region)) was folded over the other half of the PC film along the 1st folding line, to realize the 1st fold. The next 3 folds were achieved one after another by the same water-assisted process to get a PC film with 16 layers; by trial-and-error procedure we found that this was strong enough to be peeled off from the substrate without (apparent) damage for further folding "by hand." After the 10th fold, the sample was too rigid to be folded further. This 1024-layer

sample made in this manner from the original 400 nm thick PC film was compressed (≈ 40 MPa) in a machine press with a couple of stainless steel spacers with thickness of 0.4 mm at 150 $^\circ\text{C}$ for 10 min to improve interlayer contact, yielding a sample with thickness of about 0.4 mm. It was found that the compressed "10-fold" sample could be folded for 2 more times (12 folds, Figure S3, Supporting Information). However, this sample was not further studied in this work due to sample size constraints of the mechanical three-point bending testing equipment.

To make the composite with single layer graphene on one side of the PC film, the same PC solution was first spin-coated on the monolayer graphene film on Cu foil to form a **PCG** composite film, and then it was folded for 10 times in the same manner as described above. Large-scale CVD-grown polycrystalline graphene films on Cu foils were provided by the Chongqing Institute of Green and Intelligent Technology in Chinese Academy of Sciences (Figure S13, Supporting Information). The samples made with 400 nm thick PC, or 400 nm thick PC with monolayer graphene film were: i) 10-fold pure PC films (**F-PC**); thus having 1024 layers), ii) 10-fold **PCG** films (**F-PCG**; thus having 1024 layers), iii) 1024 stacked layers of PC film (**S-PC**), and iv) 1024 stacked layers of **PCG** film in a PCG-GPC manner (**S-PCG**). All of these types of samples were hot pressed at 150 $^\circ\text{C}$ for 10 min at ≈ 40 MPa to remove gaps between each layer. 5 separate samples of each type i)–iv) were made with the same procedure so that the mechanical testing could account for experimental variance.

Characterizations: A Bruker Dimension Icon AFM instrument was used to analyze the thickness of the single layer **PCG** film. Raman spectroscopy was done with a Wi-Tec micro-Raman instrument using a 532 nm laser excitation with a spot size of 250 nm. A FEI Verios 460 SEM was used to observe the structures of the composites. A three-point bending test configuration on a dynamic mechanical analyzer (DMA Q800, TA Instruments) was done to measure the bending response of the composite samples. The dimensions of the specimens were 15 mm \times ≈ 1.1 mm \times ≈ 0.4 mm (span \times width \times thickness). The stress-strain plots were obtained with a displacement rate of 100 $\mu\text{m min}^{-1}$ and the applied force and deflection were measured.

FEM Modeling: FEM simulations replicating the three-point bending test configuration were performed to discriminate and quantify the restrain role of folding on the scaling of bending properties, independently from the material used. The material was PC following a linear elastic and isotropic constitutive behavior ($E = 2.2$ GPa, $\nu = 0.37$, $\rho = 1.21$ g cm^{-3}). The simulated plate had planar dimensions of 5.0 \times 3.5 mm^2 . The plate was supported by two rigid cylinders of radius 0.2 mm with axes orthogonal to the plate longest edge and at a mutual distance (span) of 3 mm. The load at the mid-span was applied by a third rigid cylinder (radius 0.2 mm) moving at a constant imposed velocity of 1 mm min^{-1} up to a total deflection of 1 mm. Contact algorithm was implemented between the rigid cylinder and the layers and between each layer. A conventional coefficient of friction $\mu = 0.31$ was assumed, which is an ordinary value for PC. Each layer was made of thick-shell elements with thickness 8 μm (in plane dimension 50 \times 50 μm^2 , aspect ratio 6.25) with one element through the thickness. This thickness value was the lowest that could be simulated in order to have correct contact detection and stability with the used discretization. Because of the extremely long time scale, the real fold process could not be simulated. Folds were taken into account by welding together the edge nodes of different layers in the correspondence of folds (e.g., for 1 fold, the nodes at one edge were welded, for 2 folds, 4 layers were welded at one edge, 2 couples of 2 layers each were welded at another edge, no constraint at the other edges, etc., as the reader may verify by folding a paper). To compare simulation results to experiments and theory, the bending properties were normalized with respect to the mass of the samples. Since the simulated experiment is in displacement control, the bending force was measured indirectly from the reactions at the two cylindrical supports whose sum, for static equilibrium, was equal to the external force applied by the moving cylinder. The bending stiffness was computed according to the three-point bending scheme as $D_n = \frac{EI}{w} = \frac{PL^3}{48w\delta}$.

Supporting Information

Supporting Information is available from the Wiley Online Library or from the author.

Acknowledgements

This work was supported by the Institute for Basic Science (Grant No. IBS-R019-D1). N.M.P. is supported by the European Commission under the Graphene Flagship Core 2 grant No. 785219 (WP14 “Polymer Composites”) and FET Proactive “Neurofibres” grant No. 732344 as well as by the Italian Ministry of Education, University and Research (MIUR) under the “Departments of Excellence” grant L.232/2016. The authors acknowledge financial support from the National Natural Science Foundation of China (Grant No. 51402291). S.S. acknowledges financial support from the BrainKorea21 Plus (National Science Foundation of Korea) and the Ermenegildo Zegna Founder’s Scholarship 2017–2018. This study was also supported by the Creative Materials Discovery Program (Grant No. 2016M3D1A1900038) through the National Research Foundation of Korea (NRF).

Conflict of Interest

The authors declare no conflict of interest.

Keywords

composites, folding, graphene, mechanical reinforcement

Received: December 21, 2017

Revised: May 13, 2018

Published online:

- [1] Y. Zhu, H. Ji, H.-M. Cheng, R. S. Ruoff, *Natl. Sci. Rev.* **2017**, *5*, 90.
- [2] L. Gong, R. J. Young, I. A. Kinloch, I. Riaz, R. Jalil, K. S. Novoselov, *ACS Nano* **2012**, *6*, 2086.
- [3] H. Porwal, P. Tatarko, S. Grasso, J. Khaliq, I. Dlouhy, M. J. Reece, *Carbon* **2013**, *64*, 359.
- [4] O. M. Istrate, K. R. Paton, U. Khan, A. O’Neill, A. P. Bell, J. N. Coleman, *Carbon* **2014**, *78*, 243.
- [5] A. Nieto, R. Dua, C. Zhang, B. Boesl, S. Ramaswamy, A. Agarwal, *Adv. Funct. Mater.* **2015**, *25*, 3916.
- [6] J. J. Liang, Y. Huang, L. Zhang, Y. Wang, Y. F. Ma, T. Y. Guo, Y. S. Chen, *Adv. Funct. Mater.* **2009**, *19*, 2297.
- [7] G. Goncalves, P. Marques, A. Barros-Timmons, I. Bdkin, M. K. Singh, N. Emami, J. Gracio, *J. Mater. Chem.* **2010**, *20*, 9927.
- [8] S. Vadukumpully, J. Paul, N. Mahanta, S. Valiyaveetil, *Carbon* **2011**, *49*, 198.
- [9] P. May, U. Khan, A. O’Neill, J. N. Coleman, *J. Mater. Chem.* **2012**, *22*, 1278.
- [10] M. Z. Seyedin, J. M. Razal, P. C. Innis, R. Jalili, G. G. Wallace, *Adv. Funct. Mater.* **2015**, *25*, 94.
- [11] I. Alstrup, I. Chorkendorff, S. Ullman, *Surf. Sci.* **1992**, *264*, 95.
- [12] X. Li, W. Cai, J. An, S. Kim, J. Nah, D. Yang, R. Piner, A. Velamakanni, I. Jung, E. Tutuc, S. K. Banerjee, L. Colombo, R. S. Ruoff, *Science* **2009**, *324*, 1312.
- [13] A. Reina, X. Jia, J. Ho, D. Nezich, H. Son, V. Bulovic, M. S. Dresselhaus, J. Kong, *Nano Lett.* **2009**, *9*, 30.
- [14] S. Bae, H. Kim, Y. Lee, X. Xu, J.-S. Park, Y. Zheng, J. Balakrishnan, T. Lei, H. Ri Kim, Y. I. Song, Y.-J. Kim, K. S. Kim, B. Ozyilmaz, J.-H. Ahn, B. H. Hong, S. Iijima, *Nanotechnol.* **2010**, *5*, 574.
- [15] Y.-H. Lee, X.-Q. Zhang, W. Zhang, M.-T. Chang, C.-T. Lin, K.-D. Chang, Y.-C. Yu, J. T.-W. Wang, C.-S. Chang, L.-J. Li, T.-W. Lin, *Adv. Mater.* **2012**, *24*, 2320.
- [16] P. Liu, Z. Jin, G. Katsukis, L. W. Draushuk, S. Shimizu, C.-J. Shih, E. D. Wetzell, J. K. Taggart-Scarff, B. Qing, K. J. Van Vliet, R. Li, B. L. Wardle, M. S. Strano, *Science* **2016**, *353*, 364.
- [17] I. Vlassiok, G. Polizos, R. Cooper, I. Ivanov, J. K. Keum, F. Paulauskas, P. Datskos, S. Smirnov, *ACS Appl. Mater. Interfaces* **2015**, *7*, 10702.
- [18] N. M. Pugno, *J. Mech. Phys. Solids* **2010**, *58*, 1397.
- [19] B. C. Gallivan, *How to Fold Paper in Half Twelve Times: An Impossible Challenge Solved and Explained*, Historical Society of Pomona Valley, Pomona, CA, USA **2002**.
- [20] B. Wang, M. Huang, N. Y. Kim, B. V. Cunniff, Y. Huang, D. Qu, X. Chen, S. Jin, M. Biswal, X. Zhang, S. H. Lee, H. Lim, W. J. Yoo, Z. Lee, R. S. Ruoff, *Nano Lett.* **2017**, *17*, 1467.
- [21] B. Wang, M. Huang, L. Tao, S. H. Lee, A. R. Jang, B.-W. Li, H. S. Shin, D. Akinwande, R. S. Ruoff, *ACS Nano* **2016**, *10*, 1404.
- [22] Z. C. Li, W. Zhang, X. Fan, P. Wu, C. Zeng, Z. Li, X. Zhai, J. Yang, J. Hou, *J. Phys. Chem. C* **2012**, *116*, 10557.
- [23] K. Kim, S. Coh, L. Z. Tan, W. Regan, J. M. Yuk, E. Chatterjee, M. F. Crommie, M. L. Cohen, S. G. Louie, A. Zettl, *Phys. Rev. Lett.* **2012**, *108*, 246103.
- [24] C. S. Ruiz-Vargas, H. L. Zhuang, P. Y. Huang, A. M. van der Zande, S. Garg, P. L. McEuen, D. A. Muller, R. G. Hennig, J. Park, *Nano Lett.* **2011**, *11*, 2259.
- [25] Q.-Y. Lin, G. Jing, Y.-B. Zhou, Y.-F. Wang, J. Meng, Y.-Q. Bie, D.-P. Yu, Z.-M. Liao, *ACS Nano* **2013**, *7*, 1171.
- [26] C. Lee, X. Wei, J. W. Kysar, J. Hone, *Science* **2008**, *321*, 385.
- [27] X. Chen, C. Yi, C. Ke, *Appl. Phys. Lett.* **2015**, *106*, 101907.

ADVANCED MATERIALS

Supporting Information

for *Adv. Mater.*, DOI: 10.1002/adma.201707449

Folding Large Graphene-on-Polymer Films Yields Laminated Composites with Enhanced Mechanical Performance

Bin Wang, Zhancheng Li, Chunhui Wang, Stefano Signetti, Benjamin V. Cunniff, Xiaozhong Wu, Yuan Huang, Yi Jiang, Haofei Shi, Seunghwa Ryu, Nicola M. Pugno, and Rodney S. Ruoff**

Supporting Information for

Folding Large Graphene-on-Polymer Films Yields Laminated Composites with Enhanced Mechanical Performance

Bin Wang, Zhancheng Li, Chunhui Wang, Stefano Signetti, Benjamin V. Cunning, Xiaozhong Wu, Yuan Huang, Yi Jiang, Haofei Shi, Seunghwa Ryu, Nicola M. Pugno, Rodney S. Ruoff**

Dr. B. Wang, Dr. C. Wang, Dr. B. V. Cuning, Dr. X. Wu, Dr. Y. Huang, Dr. Y. Jiang, Prof. R. S. Ruoff
Center for Multidimensional Carbon Materials
Institute for Basic Science (IBS)
Ulsan 44919, Republic of Korea

Prof. R. S. Ruoff
Department of Chemistry and School of Materials Science and Engineering
Ulsan National Institute of Science and Technology (UNIST)
Ulsan 44919, Republic of Korea
E-mail: rsruoff@ibs.re.kr; ruofflab@gmail.com

Associate Prof. Z. Li, Prof. H. Shi
Chongqing Institute of Green and Intelligent Technology,
Chinese Academy of Sciences,
Chongqing 400714, P. R. China.

Dr. S. Signetti, Prof. S. Ryu
Department of Mechanical Engineering
Korea Advanced Institute of Science and Technology (KAIST)
Daejeon 34141, Republic of Korea

Prof. N. M. Pugno
Laboratory of Bio-inspired & Graphene Nanomechanics, Department of Civil, Environmental and
Mechanical Engineering,
University of Trento,
Via Mesiano 77, 38123 Trento, Italy.
E-mail: nicola.pugno@unitn.it

Prof. N. M. Pugno
School of Engineering and Materials Science,
Queen Mary University of London,
Mile End Road, London E1 4NS, U.K.

Prof. N. M. Pugno
Ket-Lab, Edoardo Amaldi Foundation,
Italian Space Agency,
Via del Politecnico snc, 00133 Rome, Italy.

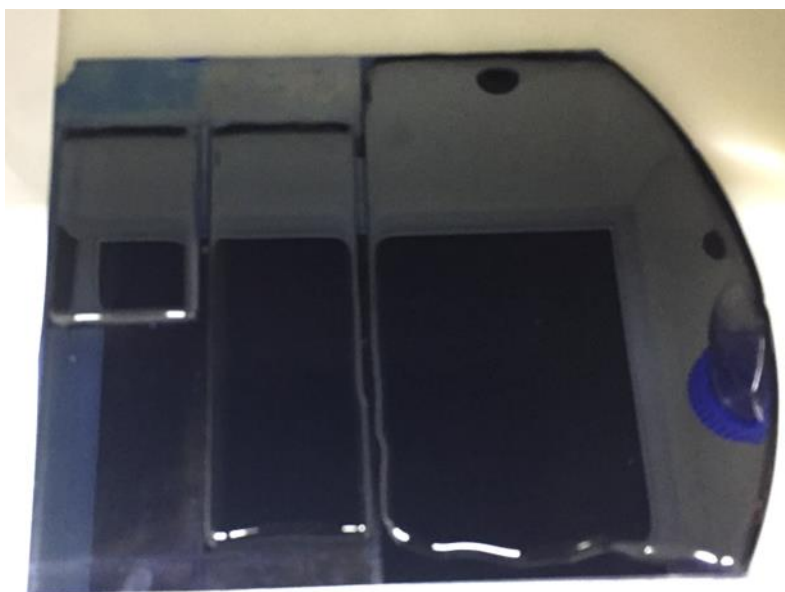


Figure S1. SAM patterned SiO₂/Si wafer showing the regions with different wettability.

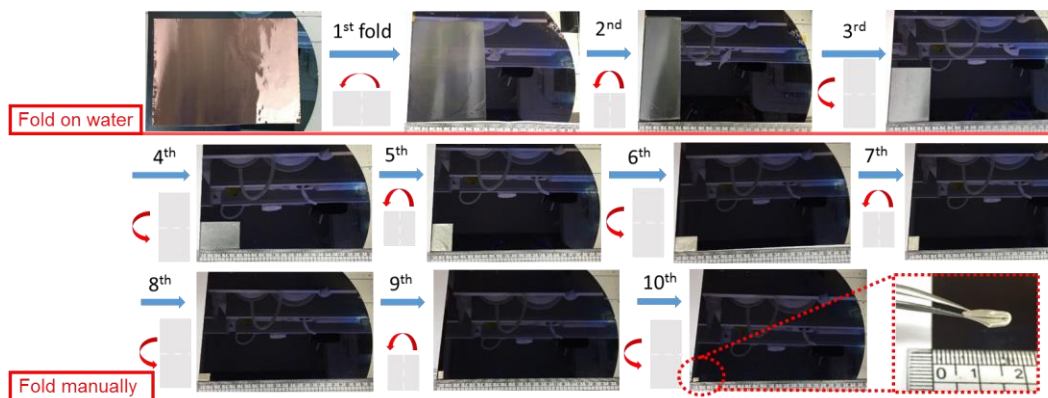


Figure S2. Photographs show the process for folding of an A5-sized, ~400nm thick PC film in half 10 times, to make a thicker material from a 2D thin film. Two steps were used to make the first 4 folds assisted by using the water, and 6 further folds were done manually in ambient conditions.

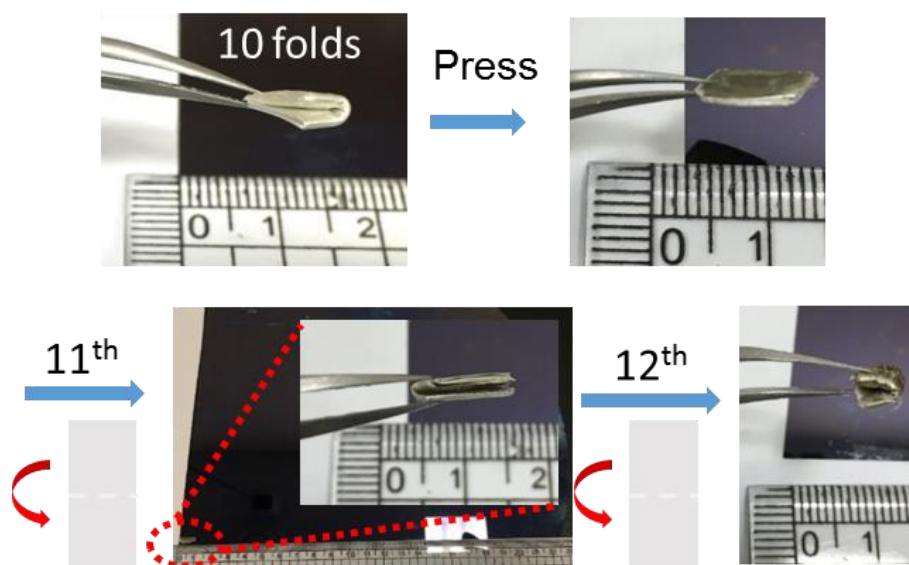


Figure S3. Compression of the 10-fold sample and two further folds made by hand to get a 12-fold sample.

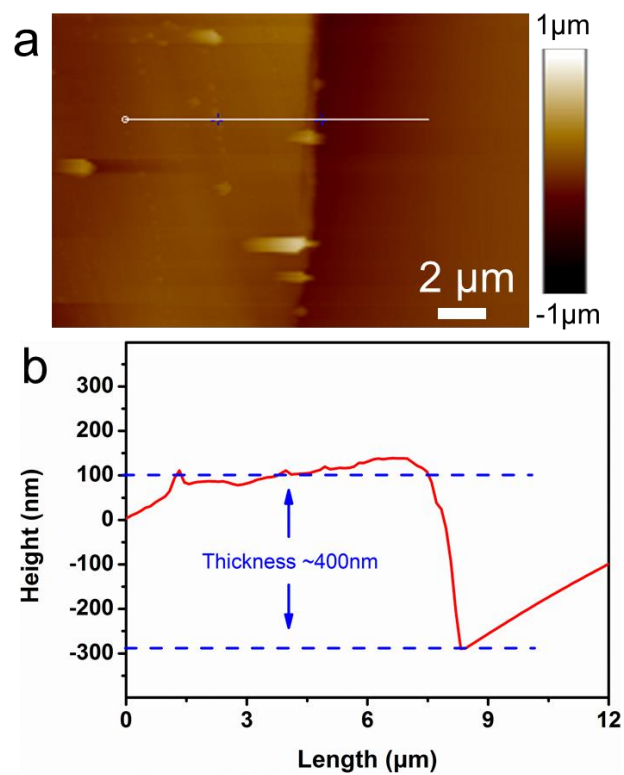


Figure S4. AFM measurement of the thickness of a single layer of PCG composite film on SiO₂/Si wafer.

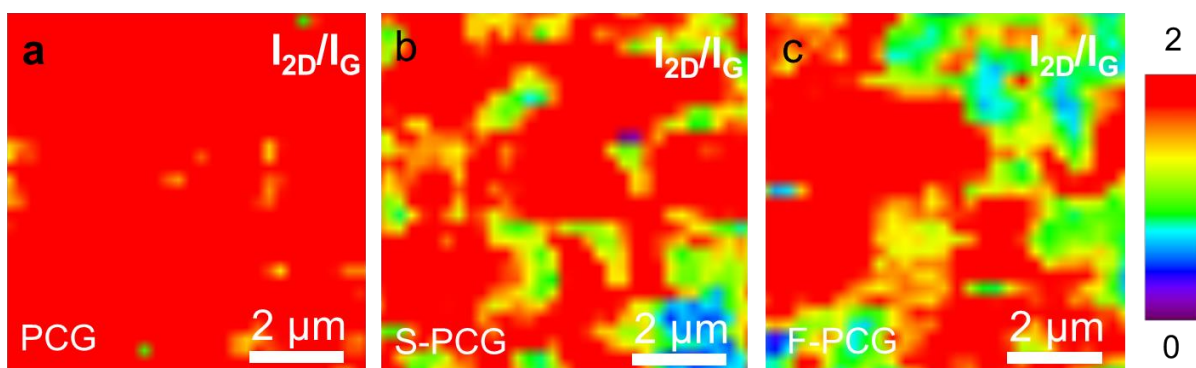


Figure S5. I_{2D}/I_G maps for (a) 1 layer PCG, (b) S-PCG and (c) F-PCG.

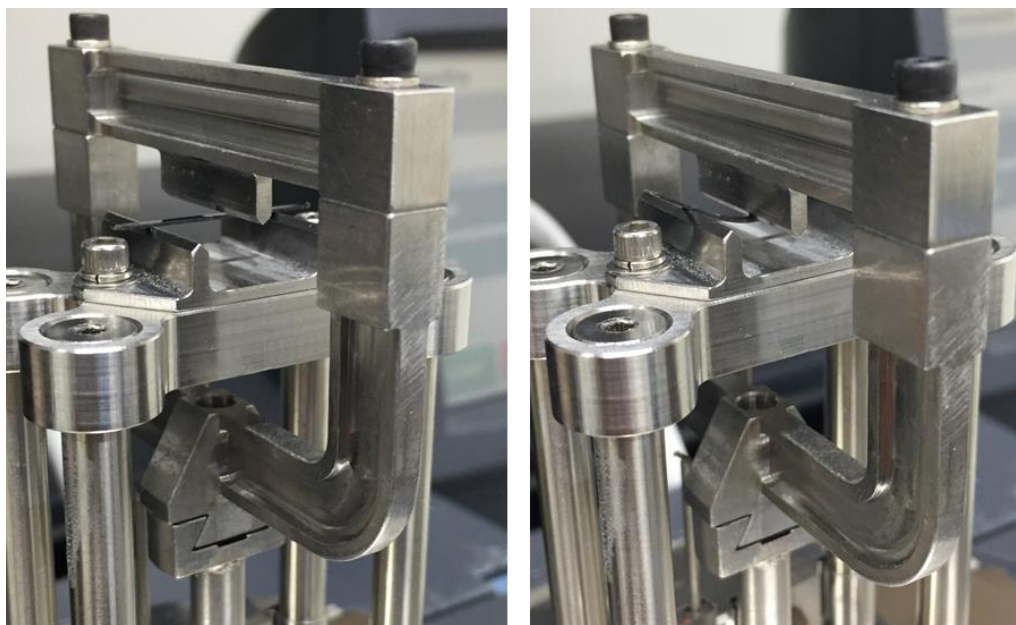


Figure S6. Three-point bending configuration on DMA Q800 Instrument, and the testing of an F-PCG sample.

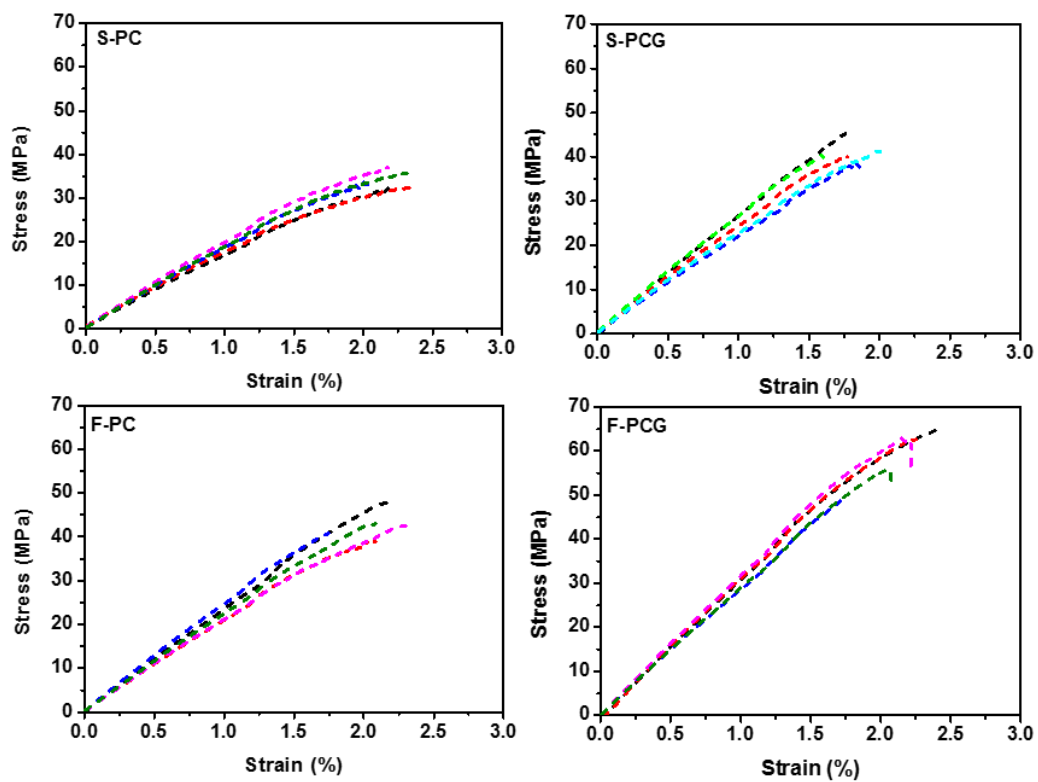


Figure S7. Stress-strain curves of the samples measured by three-point bending tests. Five specimens were measured for each sample.

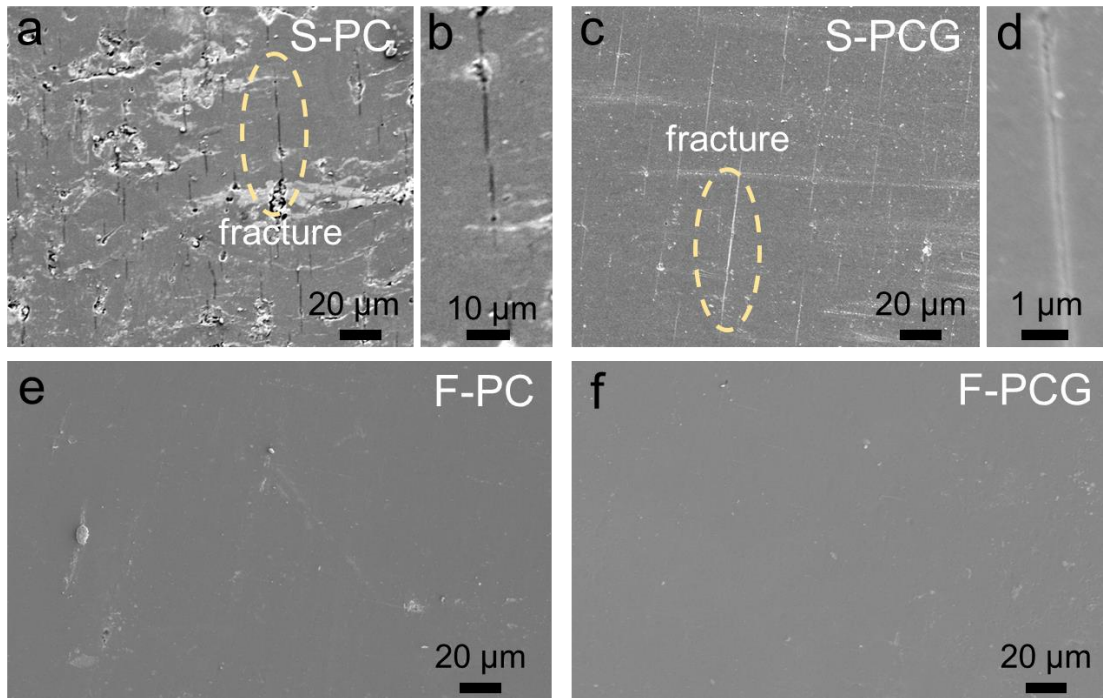


Figure S8. SEM images showing the tensed surface of the samples after the three-point bending test. Cracks appeared on the tensed chord of the bent **S-PC** (a, b) and **S-PCG** (c, d) specimens, but no cracks were observed on tensed chord of the **F-PC** and **F-PCG** samples, indicating that the failure of the stacked samples was due to cracks forming on the tensed surface (bottom chord).

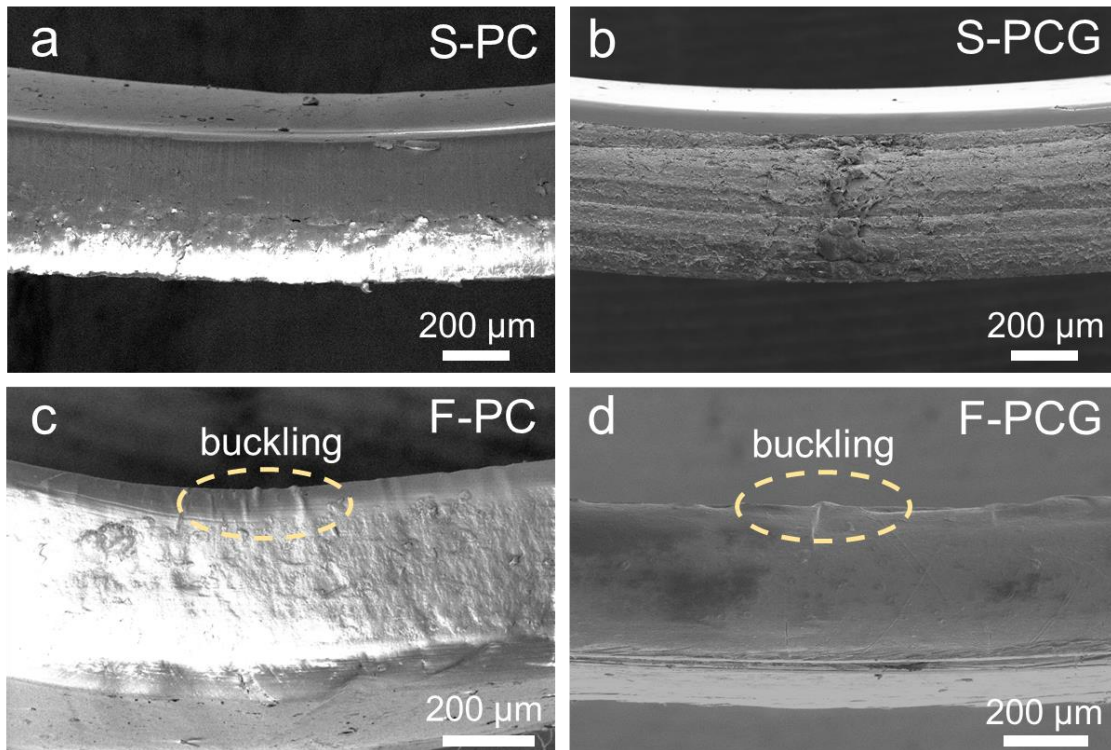


Figure S9. SEM images showing the cross section of bent samples. No local buckling was observed on the compressed chord for **S-PC** and **S-PCG** specimens, but they were present on the **F-PC** and **F-PCG** samples, indicating that the failure of the folded samples was due to the buckling on the compressed chord.

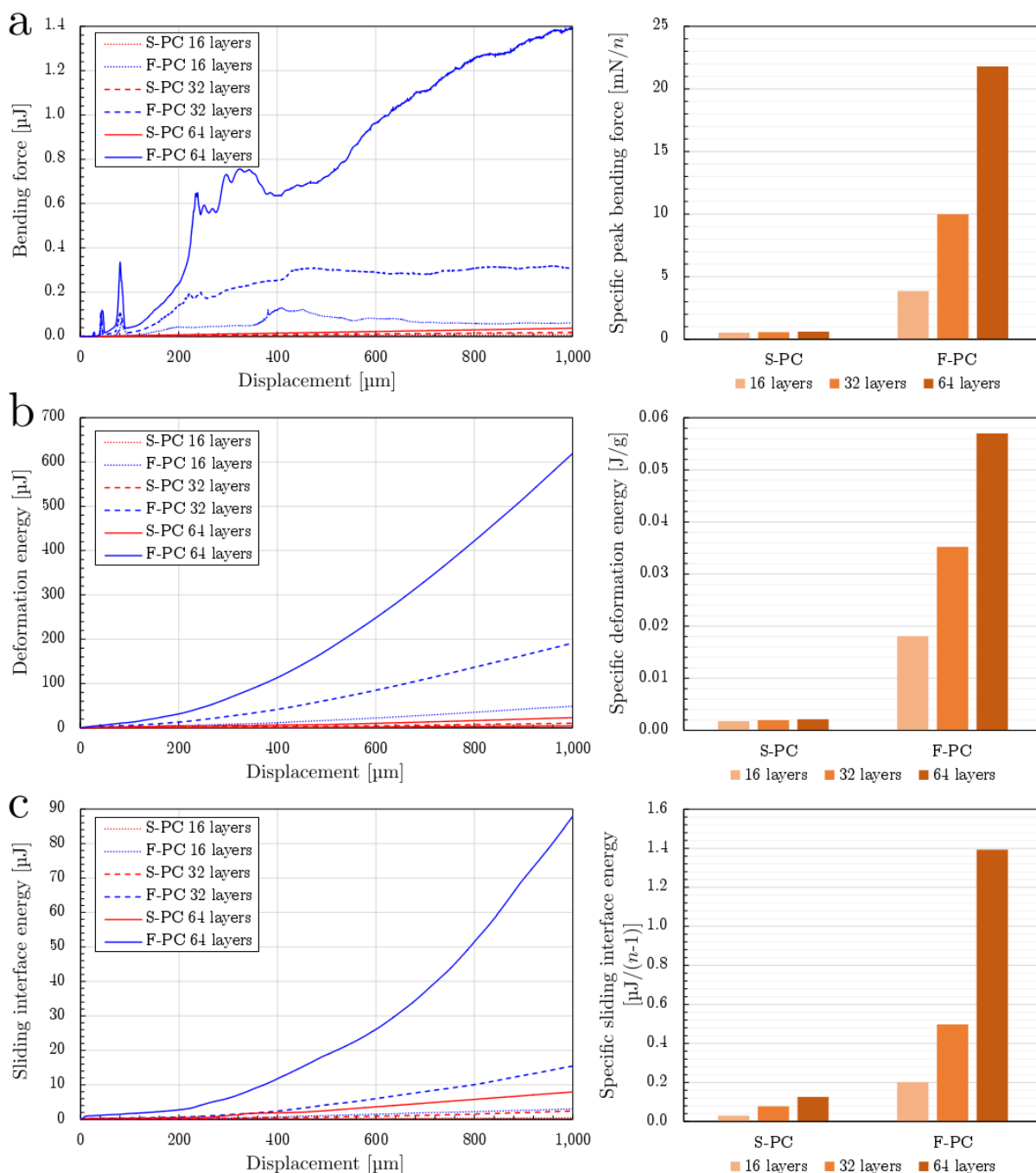


Figure S10. Additional data from simulations of 16-32-64 **S-PC** and **F-PC** samples. In the left panels the evolution of the measured quantities vs. the bending deflection are depicted; in the right panels histograms show the corresponding specific values at their recorded maximum values: (a) specific peak bending force, (b) specific deformation (strain) energy (maximum at 1 mm deflection), and (c) sliding interface (friction) energy per interface (max at 1 mm deflection).

From fitting of the simulation results we find the following scaling dependencies for the interface energy $U_{I,S-PC} \sim n^{2.060}$ and $U_{I,F-PC} \sim n^{2.429}$.

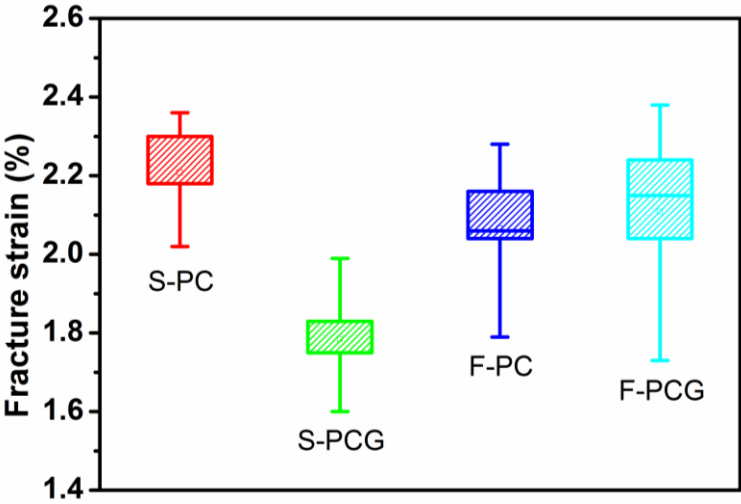


Figure S11. Comparison of the fracture strain for different samples.

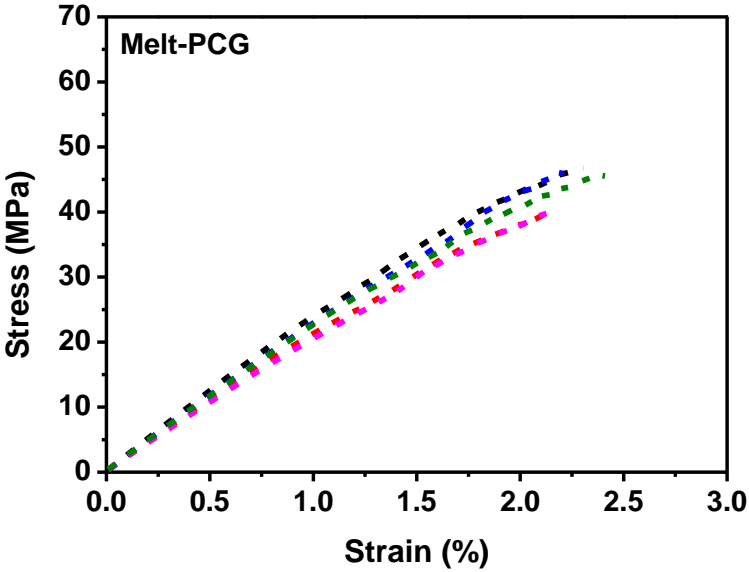


Figure S12. Stress-strain curves of the **Melt-PCG** samples measured by three-point bending tests. Five specimens of this sample type were made and measured.

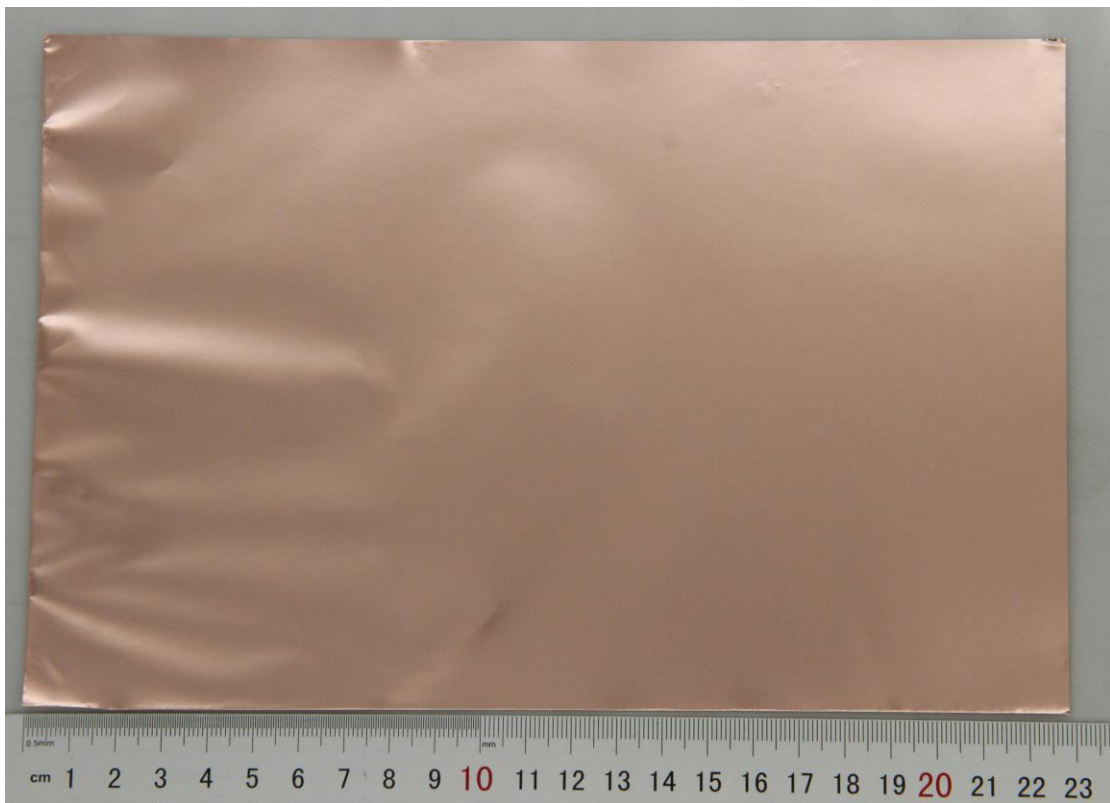


Figure S13. CVD-grown single layer graphene on an A5 sized Cu foil.

Equations: The ultimate strength, strain, and toughness modulus scale respectively as:

$$\sigma_u^{(F,G)} = \sigma_u s_\sigma f_\sigma g_\sigma \cong \sigma_u \sqrt{s_E f_E g_E s_\gamma f_\gamma g_\gamma} \quad (\text{S1})$$

$$\varepsilon_u^{(F,G)} = \varepsilon_u s_\varepsilon f_\varepsilon g_\varepsilon \cong \varepsilon_u \frac{s_\sigma f_\sigma g_\sigma}{s_E f_E g_E} = \varepsilon_u \sqrt{\frac{s_\gamma f_\gamma g_\gamma}{s_E f_E g_E}} \quad (\text{S2})$$

$$T_u^{(F,G)} = T_u s_T f_T g_T \cong T_u s_\sigma f_\sigma g_\sigma s_\varepsilon f_\varepsilon g_\varepsilon = T_u s_\gamma f_\gamma g_\gamma \quad (\text{S3})$$

where the last equations assume $\varepsilon_u \propto \frac{\sigma_u}{E}$, $T_u \propto \sigma_u \varepsilon_u$. From the previous equations the advantage to have both folding ($f > 1$) and/or graphene ($g > 1$) with respect to their absences ($f = g = 1$) is evident for stiffening (E), strengthening (σ_u) and toughening (T_u) but not for maximal strain (ε_u) that can increase or decrease depending on the square root value appearing in Equation (S2), larger or smaller than one respectively.

Model predictions: According to Equation (5) and from the ratios **F-PC/S-PC** or **S-PCG/S-PC** between the values of E for each test (**Table S2**) we can extract $f_E \cong 1.242$ or $g_E \cong 1.372$, respectively, as the average of $f_E^{(i)}, g_E^{(i)}$ determined from each measurement; the similarity between the two values confirms the self-consistency of the theory, since **S-PCG** and **F-PC** resulted in nearly the same bending stiffness D . Note also that the extracted value of g_E is in good agreement with the prediction of Equation (3) in the manuscript that yields to $g_E \cong 1.449$, with $E_g = 1$ TPa, $E_m = 1.89$ GPa (average Young's modulus of s-PC sample, see **Table S2**), $t_g = 0.34$ nm, $t_m = 400$ nm. Generally speaking, we have:

$$f_X = \frac{1}{N} \sum \frac{X_{\text{F-PC}}^{(i)}}{X_{\text{S-PC}}^{(i)}} \quad (\text{S4.a})$$

$$g_X = \frac{1}{N} \sum \frac{X_{\text{S-PCG}}^{(i)}}{X_{\text{S-PC}}^{(i)}} \quad (\text{S4.b})$$

where X denotes the considered mechanical property and N the number of tests. Applying Equations (S4) also to the strength σ_u we derive $f_\sigma \cong 1.254$ and $g_\sigma \cong 1.258$. From Equations (S1-3) it is possible to derive from the previously determined coefficients the corresponding values for the fracture strain $f_\varepsilon^d \cong 1.010$ or $g_\varepsilon^d \cong 0.881$ and for the toughening $f_\gamma^d \cong 1.267$ or $g_\gamma^d \cong 1.065$, where the superscript d indicates that the coefficients are derived independently with our model. Of course, the same can be directly derived again from experimental data by Equations (S4) and the corresponding values are $f_\varepsilon \cong 0.937$ or $g_\varepsilon \cong 0.808$ for fracture strain and $f_\gamma \cong 1.149$ or $g_\gamma \cong 0.907$ for toughness modulus, respectively. The good agreement between parameters derived from different approaches/measurements confirms the validity of our model. Computed values are reported and compared in **Table S1**. From experimental results it is then possible to derive, recalling Equations (S4), the synergy factors s_X for each mechanical property as:

$$s_X = \frac{1}{N} \sum \left(\frac{X_{\text{F-PCG}}^{(i)}}{X_{\text{S-PC}}^{(i)}} \right) / (f_X \cdot g_X) \quad (\text{S5})$$

which yields $s_E \cong 1.023$, $s_\sigma \cong 1.146$, $s_\varepsilon \cong 1.261$, and $s_\gamma \cong 1.521$. The values so calculated were used for the computation of **F-PCG** properties (4th column of **Table S2**). The experimental values of Young's modulus, fracture strength, fracture strain, and toughness modulus are reported in **Table S2** together with model predictions for each test. Note that the prediction of Young's modulus and strength for **S-PCG** and **F-PC** were done with the coefficient derived from the ratio

between experimental measurements ($f_{E,\sigma}, g_{E,\sigma}$), while the other predictions were made with the coefficient derived independently by our model ($f_{\varepsilon,\gamma}^d, g_{\varepsilon,\gamma}^d$). Thus, among the 72 model predictions reported in **Table S2**, 72-24=48 are independent and predicted on the basis of the only 4 values of $f_{E,\sigma}, g_{E,\sigma}$ and 4 synergy factors s_X . A good agreement is observed.

Table S1. Folding and reinforcement factors, f_X and g_X respectively, as computed from fit of experimental data or model predictions (Equations S1-3) and their comparison (the X indicates the mechanical property to which the factor refers). For their determination see the *Model predictions* section in the Supporting Information. Highlighted in blue the values used for the model predictions of **F-PCG** properties (column 4 in **Table S2**). In the last column the values in square brackets correspond to the one derived as combination of the model derived factors $f_{\varepsilon,\gamma}$, $g_{\varepsilon,\gamma}$.

	Data fit Eq. (S1.a)	Model derived Eqs. (6-8)		Data fit Eq. (S1.b)	Model derived Eqs. (6-8)		Model derived ($f_X \cdot g_X$)
f_E	1.242	-	g_E	1.372	-	$f_E g_E$	1.704
f_σ	1.254	-	g_σ	1.208	-	$f_\sigma g_\sigma$	1.506
f_ε	0.937	1.010	g_ε	0.808	0.881	$f_\varepsilon g_\varepsilon$	0.757 [0.890]
f_γ	1.149	1.267	g_γ	0.907	1.065	$f_\gamma g_\gamma$	1.043 [1.349]

Table S2. Mechanical properties for samples measured by three-point bending tests. Maximal values are reported in bold, average values in italics, and related model predictions in brackets. The pure model predictions are highlighted in blue. See the *Model predictions* section in the Supporting Information and **Table S1** for the factors used for the predictions here reported.

Young's modulus (GPa)	S-PC	S-PCG	F-PC	F-PCG
#1	1.75	2.78 (2.40)	2.45 (2.17)	3.43 (3.05)
#2	1.84	2.54 (2.52)	2.20 (2.29)	3.58 (3.21)
#3	1.87	2.76 (2.56)	2.52 (2.32)	3.01 (3.26)
#4	2.04	2.36 (2.80)	2.22 (2.53)	3.33 (3.55)
#5	1.95	2.45 (2.67)	2.30 (2.42)	3.05 (3.40)
Average	<i>1.89±0.11</i>	<i>2.58±0.19 (2.59)</i>	<i>2.34±0.14 (2.35)</i>	<i>3.28±0.24 (3.29)</i>
Strength (MPa)	S-PC	S-PCG	F-PC	F-PCG
#1	32.20	45.16 (38.91)	47.61 (40.39)	64.56 (55.96)
#2	32.34	40.38 (39.08)	39.33 (40.57)	62.58 (56.20)
#3	33.41	39.87 (40.37)	41.12 (41.91)	49.25 (58.06)
#4	36.91	38.26 (44.60)	42.41 (46.30)	63.04 (64.14)
#5	35.73	41.48 (43.18)	42.79 (44.82)	55.98 (62.09)
Average	<i>34.12±2.10</i>	<i>41.03±2.58 (41.23)</i>	<i>42.65±3.08 (42.80)</i>	<i>59.08±6.41 (59.29)</i>
Fracture strain (%)	S-PC	S-PCG	F-PC	F-PCG
#1	2.18	1.75 (1.92)	2.16 (2.20)	2.38 (2.44)
#2	2.36	1.75 (2.08)	2.06 (2.38)	2.24 (2.65)
#3	2.02	1.60 (1.78)	1.79 (2.04)	1.73 (2.27)
#4	2.18	1.83 (1.92)	2.28 (2.20)	2.15 (2.44)
#5	2.30	1.99 (2.03)	2.04 (2.32)	2.04 (2.58)
Average	<i>2.21±0.13</i>	<i>1.78±0.14 (1.95)</i>	<i>2.07±0.18 (2.23)</i>	<i>2.11±0.24 (2.48)</i>
Toughness modulus (MPa)	S-PC	S-PCG	F-PC	F-PCG
#1	0.40	0.41 (0.43)	0.54 (0.51)	0.86 (0.82)
#2	0.47	0.38 (0.50)	0.51 (0.60)	0.77 (0.96)
#3	0.39	0.35 (0.42)	0.41 (0.49)	0.45 (0.80)
#4	0.46	0.39 (0.49)	0.57 (0.58)	0.78 (0.94)
#5	0.48	0.46 (0.51)	0.49 (0.61)	0.62 (0.98)
Average	<i>0.44±0.04</i>	<i>0.40±0.04 (0.47)</i>	<i>0.51±0.06 (0.56)</i>	<i>0.70±0.16 (0.90)</i>

Table S3. Mechanical properties for the **Melt-PCG** samples measured by the three-point bending test. Maximal values are reported in bold whereas average values in italics.

Melt-PCG	Young's modulus (GPa)	Strength (MPa)	Fracture strain (%)	Toughness modulus (MPa)
#1	2.56	46.72	2.31	0.60
#2	2.14	39.55	2.11	0.47
#3	2.29	46.05	2.20	0.54
#4	2.11	39.81	2.11	0.46
#5	2.34	45.52	2.40	0.62
Average	<i>2.29±0.18</i>	<i>43.53±3.54</i>	<i>2.22±0.13</i>	<i>0.54±0.07</i>

Supplementary videos

- **Video S1:** FEM three-point bending simulation of 16 layers **S-PC**
- **Video S2:** FEM three-point bending simulation of 16 layers (4 folds) **F-PC**
- **Video S3:** FEM three-point bending simulation of 32 layers **S-PC**
- **Video S4:** FEM three-point bending simulation of 32 layers (5 folds) **F-PC**
- **Video S5:** FEM three-point bending simulation of 64 layers **S-PC**
- **Video S6:** FEM three-point bending simulation of 64 layers (6 folds) **F-PC**